ChemElectroChem

Chemistry Europe
European Chemical Societies Publishing
ChemElectroChem

RESEARCH ARTICLE OPEN ACCESS

In-Operando Friction Force Microscopy Reveals Degradation and Repassivation of Epitaxial Perovskites During Oxygen Evolution Reaction Under Dynamic Cycling Conditions

Muzaffar Maksumov[1,2] | Anton Kaus[3] | Karin Kleiner[4] | Felix Gunkel[3] | Rüdiger-A. Eichel[1,2,5] | Florian Hausen[1,2]

[1]Institute of Energy Technologies, Fundamental Electrochemistry (IET-1), Forschungszentrum Jülich GmbH, Jülich, Germany | [2]Institute of Physical Chemistry, RWTH Aachen University, Aachen, Germany | [3]Peter Grünberg Institute (PGI-7), Forschungszentrum Jülich GmbH, Jülich, Germany | [4]Münster Electrochemical Energy Technology (MEET), University of Münster, Münster, Germany | [5]Faculty of Mechanical Engineering, RWTH Aachen University, Aachen, Germany

Correspondence: Florian Hausen (f.hausen@fz-juelich.de)

Received: 3 November 2025 | **Revised:** 19 December 2025 | **Accepted:** 24 December 2025

Keywords: catalyst degradation | friction force microscopy | in-operando electrochemical force microscopy | oxygen evolution reaction | perovskite oxides

ABSTRACT

A detailed understanding of catalyst degradation under dynamic conditions is essential to develop improved catalysts for the oxygen evolution reaction (OER), the bottleneck for efficient electrochemical water splitting in alkaline media. Perovskite oxides represent an interesting class of OER electrocatalysts, however, the differences in their degradation and repassivation growth rate are not yet fully understood. To address this, epitaxially grown $La_{0.6}Sr_{0.4}CoO_3$ (LSCO), $La_{0.6}Sr_{0.4}FeO_3$ (LSFO), and $La_{0.6}Sr_{0.4}MnO_3$ (LSMO) have been analyzed by in-operando friction force microscopy (FFM) during cyclic voltammetry in 0.1 M KOH. Distinctly different degradation phenomena for these materials were found. Continuous topography and friction force measurements during cycling, and postcatalysis characterization, clearly demonstrated the irreversibility of the degradation process, under dynamic conditions. Specifically, LSMO develops a robust passivation layer accompanied by pronounced roughening. LSFO forms a thin, surface-limited passivating layer with better retention, and LSCO undergoes rapid near-surface conversion with a comparatively soft adlayer. It is demonstrated that the load on the tip has a strong influence on the obtained results, which is used for an attempt to calculate the repassivation rate of the different adlayers. The results elucidate how in-operando FFM can differentiate degradation mechanisms under reaction conditions in alkaline environments and between transition metals in perovskite oxides.

1 | Introduction

Water electrolysis is a key technology for producing green hydrogen [1], involving two fundamental reactions: the hydrogen evolution reaction (HER) at the cathode and the oxygen evolution reaction (OER) at the anode. Especially, for the OER, the overpotential remains significantly high, and the optimization of catalytic processes is hindered by challenges related to catalyst stability and efficiency [2]. A major issue is that typically high performance leads to fast degradation, resulting in a rapid loss of activity during electrochemical processes [3–5]. This degradation is mainly caused by amorphization or dissolution of active sites, morphological and phase changes, bulk degradation and surface passivation [6–9].

Several studies identified perovskite oxides as a versatile and highly active class of OER catalysts in alkaline media, with the advantage of being flexible in chemical, electronic, and

electrochemical properties [10–18]. In such perovskites with ABO_3 composition, the A-site is predominantly occupied by rare earth and alkaline earth elements, while the B-site is mainly filled by transition metals [18]. Changing the B-site from one transition metal to another, or adding dopants, often results in differences in activity, stability, and degradation pathways [12, 19–21]. Under alkaline OER conditions, near-surface transformations have been reported, including A-site cation leaching (e.g., Sr^{2+}) with formation of A-site hydroxides (e.g., $La(OH)_3$), B-site oxyhydroxides (e.g., CoOOH, FeOOH), oxygen nonstoichiometry, and surface reconstruction [22]. However, simultaneous monitoring of degradation induced variations of the OER catalyst´s topography and interfacial mechanical response under reaction conditions is scarce [23–26].

In-operando friction force microscopy (FFM), an atomic force microscopy (AFM) based technique, enables real-time monitoring of both, surface topography and frictional forces as a function of applied potentials, when implemented in a three-electrode electrochemical cell [27]. Friction has been revealed to be sensitive to even subtle changes of structural and chemical properties and thus can be used to elucidate catalyst degradation and hydroxide/oxyhydroxide formation. Figure 1 depicts such an approach. Topography and friction, deconvoluted from the vertical and lateral deflection of the cantilever, respectively, are simultaneously mapped as shown in Figure 1a during cyclic voltammetry (CV) (Figure 1b). As illustrated in Figure 1c, the entire cantilever is immersed in the electrolyte.

A recent investigation of cobalt- and iron-based perovskite oxides under OER conditions revealed differences between surface and bulk degradation [28], where X-ray diffraction (XRD) and near-edge X-ray absorption fine structure (NEXAFS) measurements were used to follow changes in the B-site electronic structure and to identify degraded layers. These spectroscopic insights are the basis for interpreting friction contrasts and surface morphologies. However, a detailed microscopy study to unravel the impact of different transition metals on the degradation and repassivation is required. In this study, epitaxially-grown $La_{0.6}Sr_{0.4}CoO_{3-\delta}$ (LSCO), $La_{0.6}Sr_{0.4}FeO_{3-\delta}$ (LSFO), and $La_{0.6}Sr_{0.4}MnO_{3-\delta}$ (LSMO) on Nb(0.5 wt.%):$SrTiO_3$ (Nb:STO) substrates were investigated as model catalysts in alkaline media. The aim is to visualize morphological and chemical surface changes by in-operando FFM. Furthermore, the observed influence of the tip on degradation is critically discussed and used to quantify the growth rate of the passivation layers.

2 | Experimental Section

2.1 | Thin Film Fabrication

Epitaxial thin-film samples of LSCO, LSFO, and LSMO with a thickness of 15 nm were grown on $0.5 \times 10 \times 10\,mm^3$ sized (001) oriented single-crystalline, epi-polished Nb(0.5 wt.%):$SrTiO_3$ (Nb:STO) substrates (Shinkosha Co. Ltd., Yokohama, Japan), respectively. Deposition was achieved using reflection high-energy electron diffraction (RHEED)-controlled pulsed laser deposition (PLD) under an oxygen partial pressure of 0.053 mbar. The deposition parameters included a growth temperature of 650°C and a laser fluence of 2.9 $J{\cdot}cm^{-2}$ for LSCO, 2.2 $J{\cdot}cm^{-2}$ for LSFO, and 1.1 $J{\cdot}cm^{-2}$ for LSMO, employing a repetition rate of 5 Hz. The system utilized a nanosecond KrF-excimer laser with a wavelength of 248 nm. The distance maintained between the ceramic target and the heated substrate was 55 mm during the PLD process.

2.2 | Crystal Structure Analysis

The crystal structure of the perovskite catalysts was characterized by XRD (D8 Discover, Bruker AXS GmbH, Germany) by symmetric 2θ-ω scans. The diffractometer was equipped with a Goebel mirror, and a Cu anode monochromized for $K_{\alpha 1}$ radiation with a wavelength of 1.54 Å. The structural quality and phase purity of the LSCO, LSFO, and LSMO thin films were confirmed and the respective diffractograms are provided in Supporting Information (SI), Figure S1. For LSCO and LSFO, a more detailed structural and spectroscopic characterization (including XRD and NEXAFS of identically grown films) has been reported previously and

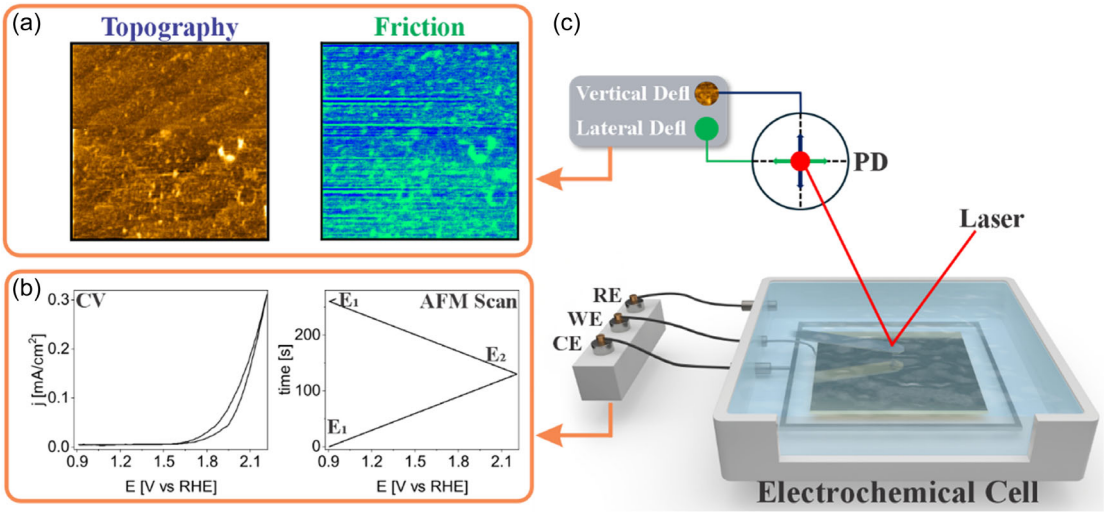

FIGURE 1 | (a) Topography map and friction force map of a perovskite oxide surface, immersed in 0.1 M KOH under dynamic potential conditions; (b) cyclic voltammetry and time versus voltage graph; and (c) schematic of the in-operando FFM set-up. Here, RE, WE, and CE are reference, working, and counter electrodes, respectively; PD–position-sensitive detector, reads the laser position reflected from cantilever.

confirms the expected perovskite phase and B-site valence states under OER-relevant conditions [28].

2.3 | In-Operando Electrochemical Friction Force Microscopy (FFM)

The surface morphology and friction force changes were investigated using FFM (AFM Dimension Icon, Bruker, Santa Barbara, USA) operated in contact mode with PPP-Cont cantilevers (Nanosensors GmbH, Switzerland). Cantilevers were individually calibrated to determine their normal and lateral spring constants based on thermal tuning procedures [29]. Absolute lateral forces F_L were obtained from the lateral force values L_T and L_R in trace and retrace direction, respectively and converted according to [30]

$$F_L = \frac{(L_T - L_R)}{2} \cdot \frac{3}{2} \cdot \frac{h \cdot k_L}{L} \cdot S_N$$

with S_N the deflection sensitivity probed inside the electrolyte (nm/V) and k_L lateral spring constant (N/m). The tip height h (13 µm) and cantilever length L (455 µm) were taken from the manufacturer's specifications. The applied normal load in all measurements was set to $F_N = 10$ nN. A fresh, uncoated tip was used for each material. Typical scan parameters were $2 \times 2\ \mu m^2$ and $10 \times 10\ \mu m^2$, scan rate was 0.872 Hz.

Measurements at reduced normal loads showed that the reconstructed adlayer (AL) on LSCO could not be removed within 30 cycles at $F_N = 5$ nN [28], whereas at $F_N = 10$ nN, as applied in this work, results in displacing the soft AL occurred while the underlying terrace structure remained intact. A load of 10 nN was therefore selected and was kept constant for all three compositions to allow a direct comparison of their frictional response and apparent repassivation behavior.

In-operando electrochemical FFM of the thin-film electrodes was performed in a home-built electrochemical cell made from chemically resistant Kel-F in 0.1 M KOH (Sigma-Aldrich, 99.99%) in deionized water (Milli-Q, > 18.2 MΩ cm). The potentiostat (BioLogic SP-300, France) was connected via a Pt wire (99.9%, MaTeCK, Germany) to the backside of the substrate, fixed by conductive carbon tape. Possible parasitic currents at exposed edges cannot be fully excluded and were treated as a minor systematic background. A separate Pt wire and an Ag|AgCl electrode (3.5 M KCl, DRIREF-2SH, World Precision Instruments GmbH, Friedberg, Germany) were used as counter and reference electrodes, respectively. All potentials in this manuscript are reported against reversible hydrogen electrode (RHE) at T = 25°C and pH = 13, according to $E_{RHE} = E_{Ag|AgCl} + E^o_{Ag|AgCl(KCl)} + 0.059 \times pH$ ($E^o_{Ag|AgCl(KCl)} = 0.1976$ V). Uncompensated resistance was expected to be low due to low current densities and small areas under investigation, thus, no iR correction was applied. CV cycles were performed at room temperature with a sweep rate of $10\ mV\ s^{-1}$; the entire $10 \times 10\ mm^2$ film was exposed and was used for current density calculations.

The PySPM library package to handle scanning probe microscopy and Bruker AFM raw data implemented from GitHub into Spyder Environment of Python software package and modified as a self-developed script was used for analysis of friction calculations of EC-FFM measurements and current/potential channels of outputs from potentiostat [31]. The Gwyddion software was used for flattening (polynomial fit first order) and correcting topography images [32]. The flattening and line correction functions were not applied to the calculated friction images.

3 | Results and Discussion

3.1 | Pristine Surface at Open Circuit Voltage

To assess whether LSCO, LSFO, and LSMO perovskite thin films (confirmed by XRD, SI, Figure S1) are prone to degradation without any applied electrode potential, the samples were immersed in 0.1 M KOH and allowed to stabilize at open circuit voltage (OCV) for 2 h. During this resting time the OCV value remains constant. Figure 2a–c show atomically smooth step-terrace morphologies and a uniform friction contrast is recorded after this period. Throughout the manuscript, color coding to differentiate the different samples is used, being blue for LSCO, green for LSFO, and red for LSMO. These observations confirm that all perovskite oxide samples remain chemically unchanged without externally applied potentials in the electrolyte. The root mean square roughness (RMS) is 1.08 , 0.54, and 0.45 nm for LSCO, LSFO, and LSMO, respectively. Differences in RMS across the three materials might reflect terrace-width variations [28]. Figure 2d presents friction probability density (nN^{-1}) revealing average forces of 8.92 ± 3.66 nN for LSMO and 11.32± 4.92 nN for LSFO, whereas LSCO exhibits a consistently higher value of 23.57 ± 11.42 nN. Please note that this is also reflected in the color scale bars of the friction images. On LSCO, two large protrusions (label i) with friction of 28.00–33.60 nN locally obscured terrace

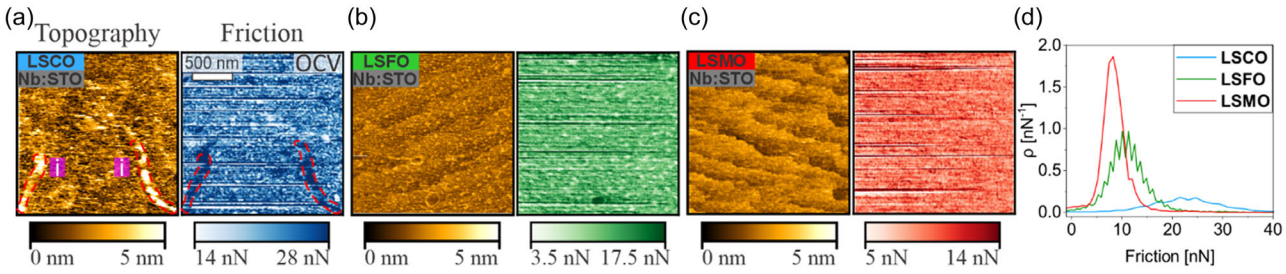

FIGURE 2 | Topography and friction images of $2 \times 2\ \mu m^2$ of (a) LSCO, (b) LSFO, and (c) LSMO at OCV in 0.1 M KOH; (d) friction probability density of the respective friction values. A uniform friction is observed in all cases. Please note that the color scales are identical for topography but differ for the friction maps (LSCO: blue, LSFO: green, LSMO: red). All FFM images in this figure share the same lateral scale (scale bar shown in friction map of LSCO).

visibility. A cross-section comparison of LSCO terraces at OCV and in air confirmed the presence of terraces (cf. SI, Figure S2).

3.2 | Electrochemical Performance During 30 Cycles

To elucidate the degradation behavior under dynamically applied potentials, FFM images were recorded during 30 CV sweeps between 0.9 and 2.2 V versus RHE. Figure 3a–c show the 30 CVs during the degradation of LSCO, LSFO, and LSMO catalysts, respectively, exhibiting oxidation and reduction peaks for LSCO and LSFO, while LSMO shows primarily oxidation features. This demonstrates distinct degradation behavior of all samples and is consistent with literature [28, 33].

Figure 3d shows the normalized peak current density taken from the CVs on the anodic sweep of cycle n, $\varphi_n = j^n_{max}/j^1_{max}$, plotted against the cycle number. LSCO exhibits a very strong deactivation in the first cycles with φ_5 decaying to 0.36 by the 5th cycle. The activity of LSMO decreased less pronounced to $\varphi_5 = 0.84$ by the 5th cycle, while for LSFO a moderate initial decrease was observed ($\varphi_5 = 0.71$). Furthermore, all samples stabilize on a quasisteady regime at the 15th cycle with $\varphi_{15} = 0.31$, 0.42, and 0.31 for LSCO, LSFO, and LSMO, respectively. Therefore, cycles 1, 5, 15, and 29 were highlighted to capture early drop, quasistabilization, and the late-state behavior.

The relative ordering of the maximum OER currents in Figure 3 differs from activity trends reported for powder-based perovskites, where Co-based compositions are typically more active [34]. For identically grown LSCO and LSFO films measured with well-defined metallic contacting in a rotating disk electrode (RDE) configuration, higher intrinsic activity of LSCO relative to LSFO has been demonstrated previously [28]. In the present in-operando FFM configuration, the thin films are electrically contacted through the substrate from the backside. In this geometry, the measured current can be influenced by series resistances associated with the electrical contacting and the film-substrate interface resistances [35], which may vary between samples and are not independently quantified under these conditions. Therefore, the electrochemical data are interpreted here in terms of relative degradation and repassivation behavior under identical thin-film and contacting conditions, rather than as an absolute activity benchmark across compositions.

The CV curves in Figure 3a–c and the corresponding normalized maximum current densities φ_n in Figure 3d were obtained from the same in-operando experiments for which the FFM data in Figures 4–6 were recorded. This ensures a direct correlation between the electrochemical response and the simultaneously imaged surface evolution. Additional CV measurements on sister samples and at different normal loads (5 nN) under otherwise identical electrochemical conditions showed qualitatively similar decay trends in φ_n for each material. These further experiments confirm that the behavior in Figure 3 is representative, but they are not included in the quantitative analysis.

3.3 | Surface Evolution

The formation and evolution of reconstructed surface layers at the catalyst–electrolyte interface are expected to govern activity and durability on perovskite oxides [25, 36]. Oxyhydroxide formation, oxygen nonstoichiometry, and A-site cation redistribution are expected to differ among the LSCO, LSFO, and LSMO samples, owing to distinct B-site electronic structures and defect chemistries [19, 28]. To address this, the surface evolution as evaluated by FFM of each material is examined separately in the following sections.

3.3.1 | LSCO

Figure 4 summarizes the LSCO surface evolution during the (a) 1st, (b) 5th, (c) 15th, and (d) 29th cycles. In the 1st cycle, grain-like features (ii) nucleated on the terraces upon exceeding 1.53 V versus RHE during the anodic sweep (0.9 → 2.2 V) as indicated by the red dashed line. Such structures persist also during the cathodic sweep (2.2 → 0.9 V). The simultaneously recorded friction map revealed predominantly lower lateral forces on the newly formed grains (ii) than on the surrounding terraces, with exception of structure (i). Variations in friction compared to friction on terraces indicates the formation of near-surface reaction phases, which is consistent with literature reports of a Co-oxyhydroxide-rich layer together with A-site-rich hydroxide precipitates under alkaline operation [11, 22, 28, 37]. Initial surface changes differ slightly compared to recent reports [28]. This effect is attributed to the higher normal load of 10 nN used in this study in comparison to only 5 nN in the former study, and this influence will be discussed more critically below.

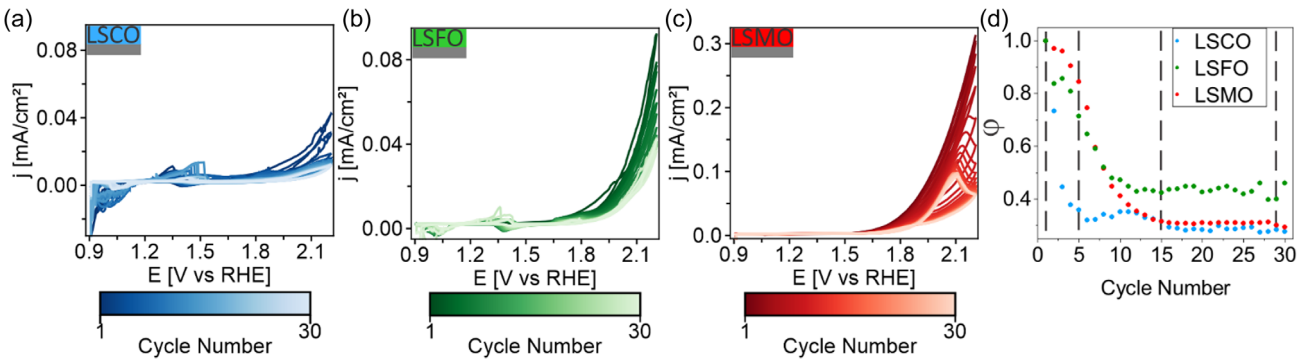

FIGURE 3 | All thirty CV cycles are shown in (a) for LSCO, in (b) for LSFO, and in (c) for LSMO, exhibiting a clear decrease in current density over cycle numbers for all samples. (d) Normalized maximum current $\varphi_n = j^n_{max}/j^1_{max}$ density of samples versus cycle numbers, j_{max} taken at 2.2 V. The curves shown correspond to the same operando experiments from which the FFM data in Figure 4–6 were acquired and thus represent one representative measurement per composition.

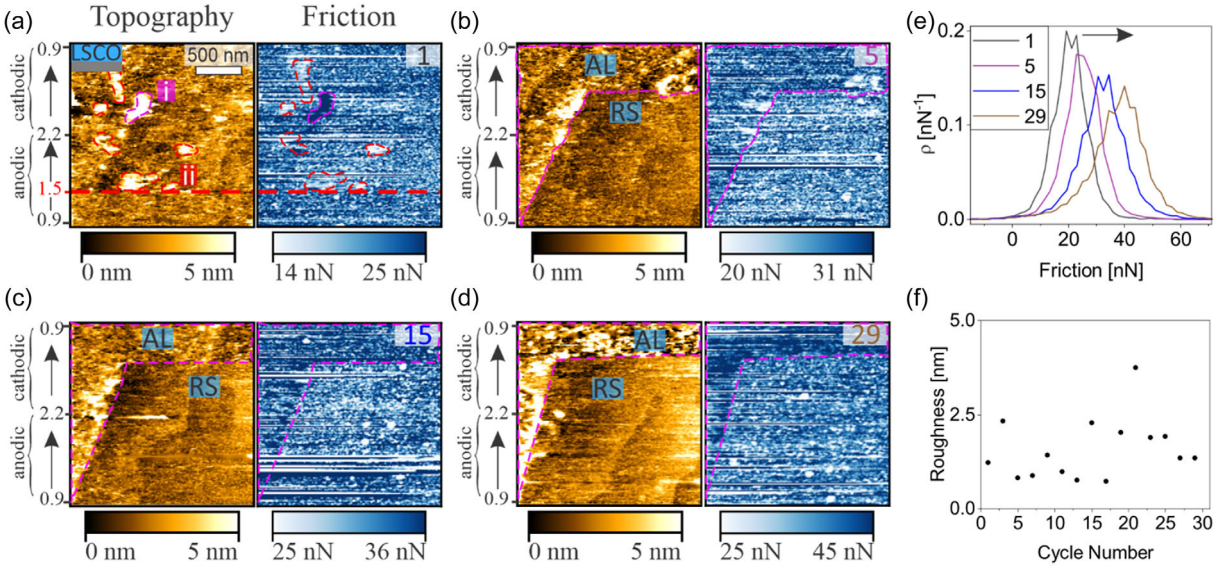

FIGURE 4 | In-operando AFM topography and friction of LSCO during (a) 1st, (b) 5th, (c) 15th, and (d) 29th cycle, (e) friction probability density of the full images of the respective cycles, i.e., including AL and RS; and (f) roughness versus cycle number. All FFM images in this figure share the same lateral scale (scale bar shown in topography map of 1st cycle). Color scales of the friction maps are adjusted per panel to the respective data range; absolute friction values are given in the friction probability density graph.

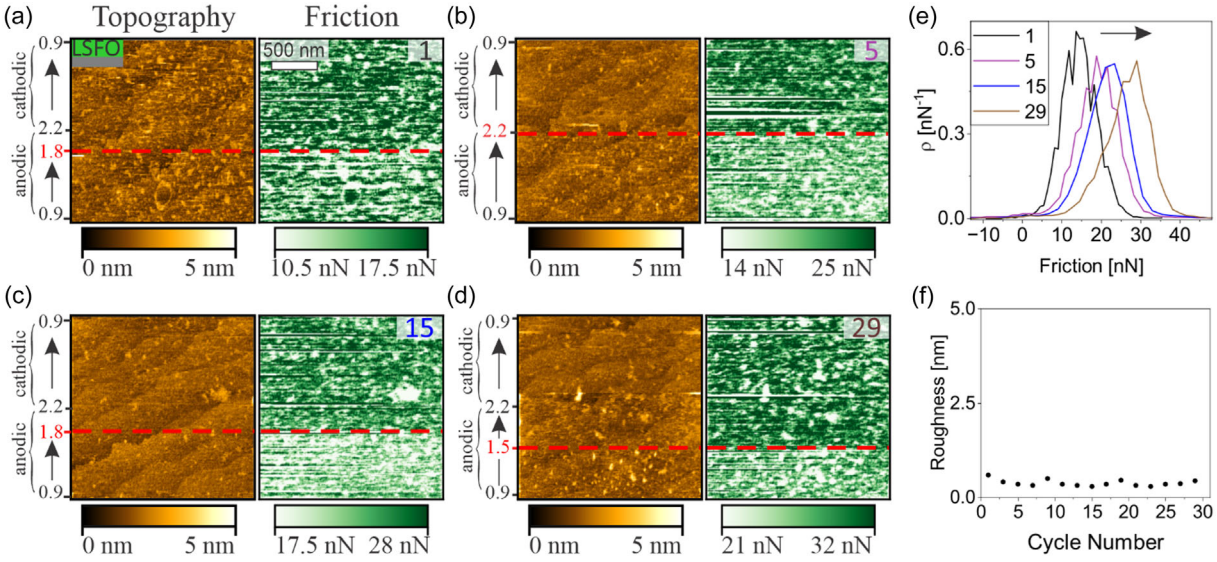

FIGURE 5 | In-operando AFM topography and friction of LSFO during (a) 1st, (b) 5th, (c) 15th, and (d) 29th cycle, (e) friction probability density of the full images of the respective cycles, i.e., including AL and RS; and (f) roughness versus cycle number. All FFM images in this figure share the same lateral scale (scale bar shown in friction map of 1st cycle). Color scales of the friction maps are adjusted per panel to the respective data range; absolute friction values are given in the friction probability density graph.

Figure 4b shows that by the 5th cycle ($\varphi_5 = 0.36$; cf. Figure 3d), a continuous, rough AL with a RMS of 1.58 nm is formed. This is only visible in the left and top parts of the image, as the 10 nN normal load yields a displacement of the AL along the scan path, producing a "removed strip" (RS) on the surface. This observation is evidenced by appearance of the pristine sample's terrace structure and a low roughness (RMS = 0.67 nm). The reason why an AL is partially observed is that the RS can only be observed in the subsequent image and the sample is subject to drift, which becomes important in section 3.4. Lateral-force maps reveal a friction offset (ΔF_L) between AL and RS of 11.2 nN, and friction fluctuations within the AL are consistent with a laterally heterogeneous, multiphase near-surface film [22]. Figure 4c verify that in the quasisteady state regime (>15th cycle) similar AL (RMS = 1.48 nm) and RS (RMS = 0.68 nm) are observed. The average friction value of 15th cycle increases relative to the 5th cycle while φ_{15} changed slightly (cf. Figure 3d), and ΔF_L increased to 14.00 nN. Differences in terrace registry relative to Figure 4b demonstrates the lateral drift, such that a previously unscanned surface was probed and the AL is visible. Figure 4d shows that during the 29th cycle, the AL continues to grow, indicated by the brighter colors, and becomes rougher (RMS = 2.28 nm). The RS part remains showing the pristine terrace structure. The average friction further increases, as illustrated in

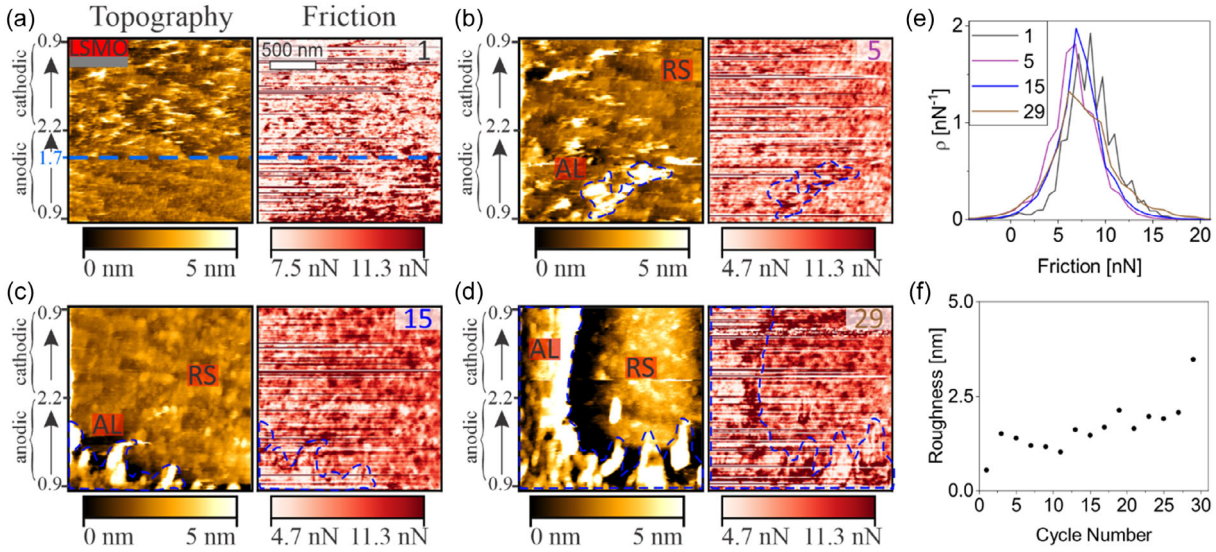

FIGURE 6 | In-operando AFM topography and friction of LSMO during (a) 1st, (b) 5th, (c) 15th, and (d) 29th cycle, (e) friction probability density of the full images of the respective cycles, i.e., including AL and RS; and (f) roughness versus cycle number. All FFM images in this figure share the same lateral scale (scale bar shown in friction map of 1st cycle). Color scales of the friction maps are adjusted per panel to the respective data range; absolute friction values are given in the friction probability density graph.

Figure 4e and ΔF_L reached 19.60 nN. Several effects might be accounted for this: either the increase in ΔF_L is predominantly caused by the larger mass of more AL that is removed under the tip, or it is influenced by sample dissolution into the electrolyte and by the formation of reaction layers [38, 39]. It has been reported that LSCO, in addition to AL formation, leaches selectively ions at higher anodic potentials during OER [22, 37]. It can thus be concluded that removal of the AL and reaction of re-exposed terraces with the electrolyte are accompanied by ion leaching and hence influence friction. Figure 4f shows the evolution of surface roughness across cycles, calculated of the entire image, and is characterized by an overall plateau with sporadic high values that could arise from accumulation of displaced AL during certain cycles. A recurring small AL region in the upper-left corner of the image across cycles 5, 15, and 29, together with differences in terrace registry, indicates a net lateral drift in the upper left direction relative to the 1st cycle frame, as sketched in Figure S4a). The repassivation growth of the surface in the RS during the scans 1–30 in the presence of wear and drift is quantified in the next section 3.4.

3.3.2 | LSFO

Figure 5 summarizes the LSFO surface evolution during the (a) 1st, (b) 5th, (c) 15th, and (d) 29th. In the 1st cycle, the step-terrace morphology is retained during the entire anodic and cathodic sweep. Interestingly, at an applied potential of 1.8 V, the friction increases from 10.55 to 17.57 nN (red dashed line) with no discernible topographic change. This is in agreement with the electrochemical behavior shown in Figure 3d, where a slower decrease in current density compared to LSCO is found. However, particle-like AL features composed of oxyhydroxide/hydroxide phase mixtures have been reported to appear around 1.7 V and to persist into the cathodic sweep within the 1st cycle, with a tendency to be displaced at even low normal loads [28]. Therefore, either no ALs are formed on LSFO, or it might be concluded that the AL is completely removed under the influence of the tip using a normal load of 10 nN as in the present experiment. The formation of oxyhydroxide phases have been reported to alter interfacial shear strength [39, 40], and hence, an increase in friction at the potential of initial AL formation would be expected, even if the layer were mechanically removed. A constant friction value after the initial increase evidences the irreversibility of the surface modifications during the first cycle [28].

Figure 5b reveals that in the 5th and 15th cycle the displacement of AL by the tip continues, as entire frames exhibit terraces as of the pristine surfaces. Differences in the terrace registry relative between the cycles indicate lateral drift as observed similarly in LSCO. The apparent shift of the friction transition in individual cycles from 1.7 to 2.2 V is attributed to drift and spatial variations to previously unscanned regions, rather than by a change in electrochemical onset.

The situation only changes slightly in the 29th cycle as illustrated in Figure 5d, although the electrochemical data shown in Figure 3d reveals a significant loss in current density of the sample. Thus, it is very likely that a passivation layer is removed rather than none is formed, in agreement with earlier reports [28].

An increase in absolute friction across cycles was observed, as shown in Figure 5e, consistent with the trend found for LSCO. For LSFO, selective ion leaching (Sr^{2+} and Fe^{2+}) at higher anodic potentials during OER has been reported in addition to passivating AL formation [28, 41, 42]. Accordingly, the increase in friction with cycle number is explained by the removal of AL together with concomitant leaching of ions. Figure 5f shows that the surface roughness across cycles remains low, consistent with a displacement of AL from the scanned area over cycles 1–30. The RS repassivation growth rate is discussed in the following section 3.4.

3.3.3 | LSMO

Figure 6 depicts the surface evolution of LSMO during the (a) 1st, (b) 5th, (c) 15th, and (d) 29th. In the 1st cycle small grains are observed to nucleate at 1.7 V (blue dashed line) and an initial

roughening of the surface is found with RMS values of 0.43 nm increasing to 0.88 nm. Importantly, the initial morphology is not recovered during the cathodic sweep, revealing an irreversible surface modification within the examined window. The change of friction occurred at the same potential as the topography change: friction decreased from 11.26 nN on terraces to 7.51 nN on the elevated structures during the anodic sweep. Prior studies using LSMO suggest the formation of a complex mixture of oxides and A-site hydroxide AL during OER [33, 43, 44]. These structures will influence friction, although friction is typically enlarged with higher roughness.

By the 5th cycle (φ_5= 0.84, cf. Figure 3d, shown in Figure 6b, a rough AL (RMS = 1.22 nm) is observed along with some removed parts that might appeared in the cathodic sweep. The comparison between individual cycles indicates that the LSMO had a net drift from right to left relative to the 1st cycle image. Friction on AL showed two different friction values, consistent with two different mixed phases (e.g. A-site hydroxide in Mn-rich oxidized states matrix) [33, 43]. As for LSFO, apparent in-frame friction steps after 1st cycle are not assigned to electrochemical onsets because drift and surface removal can expose RS established in earlier frames.

By the 15th cycle, presented in Figure 6c, a quasisteady state regime is reached (φ_{15}= 0.31, cf. Figure 3d) and the AL exhibits RMS of 2.4 nm. The removed part remains smoother (RMS = 0.66 nm) yet consisted of particle-like island rather than atomically flat terraces. The friction of AL was 4.69 nN and on the particle-like islands 11.26 nN. A height offset of 2 nm between AL and RS was measured, indicating local thinning of the AL by the tip and exposure of particulates. Formation of these particulates might be related to the additional peak in the CV around 2.1 V (cf. Figure 3d) or due to degrading of the material deeper than the near-surface region [45]. During the 29th cycle, shown in Figure 6d, a contiguous AL (RMS = 3.24 nm) coexisted with a partially thinned RS (RMS = 2.67 nm), with average height difference of around 3 nm. Friction of respective AL and RS regions remained similar to earlier cycles, 4.69 and 11.26 nN, respectively and hence, indicate that the interfacial chemistry is stabilized by the 15th cycle, which is in agreement with the electrochemical data.

As shown in Figure 6e, and in contrast to LSCO and LSFO, the average friction remained essentially constant with cycle numbers. However, with continued cycling, stabilization of near-surface AL, and a decrease in dissolution have been reported for LSMO [33]. Consequently, the imaged structures consist of previously degraded subsurface particles rather than freshly reconstructed terraces with distinct frictional response. As a result, parameters that produced friction increases in LSCO and LSFO are not dominant for LSMO, and no net increase in friction is observed with cycling. As shown in Figure 6f, the surface roughness increased continuously with cycle number, which is consistent with progressive AL thickening and coverage growth reported for LSMO [33].

3.4 | Postcycling Morphology and Frictional Behavior after 30 CVs

The fact that the images were prone to drift is used to explore the repassivation growth after the tip has removed the ALs. Figure 7 illustrates height maps, friction maps, and the corresponding height cross-sections recorded at OCV after completion of the 30-cycle in-operando sequence. The field of view was enlarged from 2 to 10 µm to relate the local changes documented in Figures 4–6 to the overall surface state of LSCO, LSFO, and LSMO. The surrounding area that experienced the same electrochemistry without direct tip contact is referred to as the as-cycled region (ACR) and is dominated by the near-surface AL. Drift directions along the RS are indicated by arrows and a schematic is provided in Figure S4.

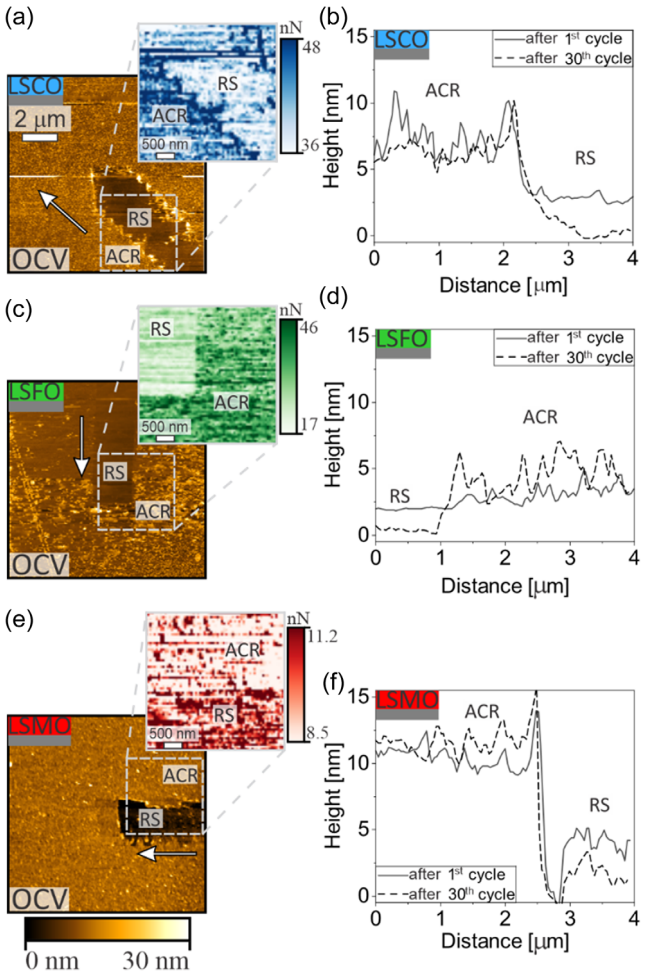

FIGURE 7 | Topography and friction images recorded at OCV after 30 CVs and their respective height cross-sections of first and last scanned positions during 30 cycles for (a,b) LSCO, (c,d) LSFO, and (e,f) LSMO. The removed strip (RS) marks the repeatedly scanned path during operando imaging, and the as-cycled region (ACR) was not tip-contacted. Arrows indicate drift direction. All FFM images in this figure share the same lateral scale (scale bars shown in topography and friction maps of LSCO).

Figure 7a reveals two clearly separated morphologies for LSCO, namely a rough ACR (RMS = 9.2 nm) and smooth RS (RMS = 2.7 nm) due to abrasion of the AL. The topographically higher edges at the rim of the previous scan consists of the removed material. The clear difference in friction between ACR (F_L = 44.16 nN) and RS (F_L = 39.23 nN) indicates their different chemistry. A height difference between ACR and RS was observed to increase from 3 to 6 nm along the drift direction, as shown in

Figure 7b. The measured height difference of 6 nm in the last scanned position might be consistent with the overall thickness of the degraded AL. A reduced height difference of 3 nm in the first scanned position indicates that the areas that were prone to tip wear effects in prior cycles repassivated on the RS when not anymore influenced by the tip. These contrasts are consistent with partial removal of a mechanically soft AL, induced by a normal load of 10 nN. Friction in the RS part exceeded the pristine friction value at OCV ($F_L = 23.57$ nN, Figure 2), indicating a chemical alteration of the re-exposed terraces due to constant removal of AL. The higher friction in the ACR suggests that chemical modification was not confined to the RS and whether this reflects globally distributed leaching of ions during cycling or local coupling to the RS cannot be distinguished here.

Figure 7c reveals a bimodal morphology for LSFO as well, exhibiting a rough ACR (RMS = 2.82 nm) and smoother RS (RMS = 0.79 nm). The friction difference between ACR (F_L = 32.06 nN) and RS ($F_L = 25.59$ nN) indicates their different chemical composition. The height difference between the ACR and RS in the last scanned position is 4 nm (Figure 7d), correlating to the overall thickness of the degraded AL as discussed for LSCO previously. The small height offset of 1.5 nm between ACR and RS at the first scan position is consistent with degradation being concentrated in a thin, surface-limited passivating AL that shields the bulk, in agreement with recent reports for LSFO [28].

LSMO shows also two different chemistries revealed by variations in friction, however, friction is higher in RS than in the ACR, unlike in LSCO and LSFO The topography images demonstrate that for LSMO the AL cannot be fully removed by an applied normal load of 10 nN since the underlying terraces are never observed after the 1st cycle, in contrast to LSCO and LSFO. Furthermore, comparing cross-sections from the last and first scanned positions of the RS to ACR in LSMO reveal height differences of 9.5–10 nm and 6.5–7.5 nm, respectively. Thus, it is concluded that the thickness of the AL in the ACR is above 10 nm and indicates partial regrowth of the first scanned position.

Because the RS occupies only a small fraction of the catalyst area (12.70, 13.14, and 8.19 μm^2 for LSCO, LSFO, and LSMO, respectively), re-exposure of catalytically active terraces in these areas are not measurably affecting the macroscopic current and hence φ_n did not increase between the cycles after the quasisteady regime reached (i.e., 15th cycle, cf. Figure 2a).

To evaluate the repassivation rate, topography cross-sections are taken along the RS between the last scanned position (point i) and first scanned position (point ii), as indicated in Figure 8a. Figure 8b–d show cross-sections, where the local height h_{RS} is plotted against the time-since-first-scan (Δt). A constant rate model, $h_{RS}(\Delta t) = h_0 + r\,\Delta t$, provides an adequate description of the data and the repassivation rate r (nm/min) is calculated as the slope of the fit. To exclude that obtained slope extracted from the RS regions shown in Figure 8 arise from image-flattening artifacts, cross-sections on the ACR of the identical images (Figure S3) are evaluated, too. For each material two ACR profiles parallel to the RS cross-section are accessed and remain horizontal. The invariance of the ACR traces confirms that the apparent RS growth must be attributed to genuine, time-dependent repassivation of the near-surface layer.

The repassivation found within the RS as shown in Figure 8b–d, demonstrate near-surface growth kinetics under given conditions

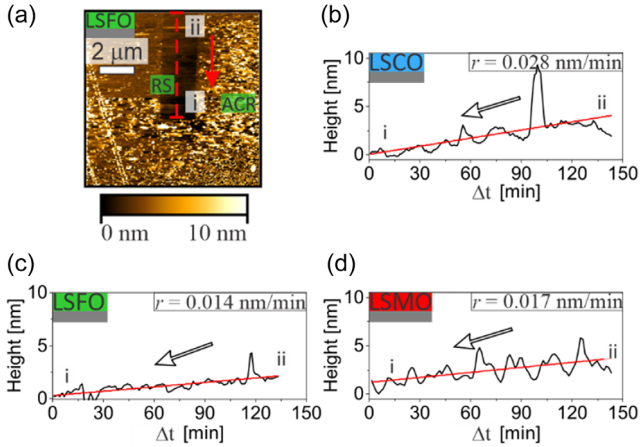

FIGURE 8 | Drift-resolved repassivation rate r: (a) Topography cross-section along the RS between the last scanned position (i) and first scanned position (ii). Linear fits of RS height versus Δt after 30 CVs for (b) LSCO, (c) LSFO, and (d) LSMO. Obtained slopes are $r = 0.028 \pm 0.002$ nm/min ($R^2 = 0.45$) for LSCO, $r = 0.014 \pm 0.001$ nm/min ($R^2 = 0.45$) for LSFO, and $r = 0.017 \pm 0.002$ nm/min ($R^2 = 0.42$) for LSMO.

and enabled a quantitative comparison across chemistries. For LSCO, h_{RS} increase monotonically with Δt, yielding r_{LSCO} = 0.028 nm/min, for LSFO $r_{LSFO} = 0.014$ nm/min, and for LSMO $r_{LSMO} = 0.017$ nm/min is observed. Overall, the fastest repassivation rate of LSCO together with an overall AL thickness of 6 nm (cf. Figure 7a,b) indicates rapid, self-limiting passivation and is consistent with strong drop in peak current density toward last cycle (Figure 3d). The slower repassivation rate of LSFO, together with an overall AL thickness of 4 nm (cf. Figure 7c,d) indicates a slower and thinner passivation AL, reflected in the higher retained current at cycle 30 (cf. Figure 3d). Despite LSMO's similar slow kinetics, the combination persistent coverage (no terrace exposure even below 10 nm) and thick overlayer capacity yields a current drop nearly as strong as LSCO by cycle 30.

The repassivation rates extracted from the drift-resolved RS height profiles in Figure 8 represent apparent growth rates of the reconstructed near-surface layer under a constant normal load of $F_N = 10$ nN. These values include both electrochemical reconstruction and the intermittent mechanical removal of the AL by the scanning tip. Hence, relative magnitudes of the rates for LSCO, LSFO, and LSMO, rather than absolute values are discussed in comparative conclusions about degradation and passivation behavior.

The chemical nature of the passivation layers is therefore inferred from the combination of the friction and topography contrasts, the electrochemical response, and the previously reported XRD and NEXAFS data on identically grown LSCO and LSFO films under alkaline OER conditions [28], together with established literature on near-surface transformations of LSMO perovskites [33]. Correlative in-operando FFM and spectroscopic studies on identical samples are considered an important direction for future work.

4 | Conclusion

In-operando FFM was applied to record topography and friction concurrently in alkaline media on OER catalysts, enabling

real-time identification of potential-dependent surface transformations. Friction was found to be a sensitive reporter of interfacial reorganization, complementing height data and highlighting changes that remained subtle in topography.

Across the LSCO, LSFO, and LSMO perovskite oxides, distinct surface-evolution pathways were resolved. On the LSCO, a heterogeneous, mechanically soft AL formed above the onset potential and was partly displaced by the scanning tip, yielding to a removed strip part. On the LSFO, an AL was also formed but readily swept from the scanned area during individual cycles, causing only terraces to be observed, accompanied by enhanced friction, consistent with a thin, passivating AL. On the LSMO, a rough AL nucleated and subsequently thickened with cycling via formation of particulates. The average friction remained stable, indicating early stabilization of the surface with continued thickness/coverage growth. Wear of AL and drift were examined to analyze the thickness of the AL for LSCO and LSFO as 6 and 4 nm, respectively, while for LSMO it exceeds 10 nm. Postcycling maps revealed material-dependent height offsets and friction contrasts between the ACRs and the worn path, evidencing time-dependent repassivation. A drift-resolved analysis of height recovery along the removed strip was further demonstrated, yielding an effective near-surface thickness growth rate r with the ordering $r_{LSCO} > r_{LSMO} \approx r_{LSFO}$.

Acknowledgments

M.M. thanks Dr. Zhenjie Teng, Dr. Julian Borowec, and Dr. Inhee Park for their experimental support and Niklas Scheer for constant support with the software design for analysis of data. The authors acknowledge funding by the German Research Foundation in the framework of the Priority Program SPP 2080 "Catalysts and reactors under dynamic conditions for energy storage and conversion", project no. **493705276.**

Open Access funding enabled and organized by Projekt DEAL.

Funding

Deutsche Forschungsgemeinschaft (493705276).

Conflicts of Interest

The authors declare no conflicts of interest.

Data Availability Statement

The data that support the findings of this study will be published after acceptance at https://doi.org/10.26165/JUELICH-DATA/PW9ZQQ.

References

1. S. Carrara, et al., Supply chain analysis and material demand forecast in strategic technologies and sectors in the EU : a foresight study. (Publications Office of the European Union, 2023), https://doi.org/10.2760/386650

2. X. Xie, L. Du, L. Yan, et al., "Oxygen Evolution Reaction in Alkaline Environment: Material Challenges and Solutions," *Advanced Functional Materials* 32 (2022): 2110036.

3. E. Fabbri, M. Nachtegaal, T. Binninger, et al., "Dynamic Surface Self-Reconstruction Is the Key of Highly Active Perovskite Nano-Electrocatalysts for Water Splitting," *Nature Materials* 16 (2017): 925–931.

4. C. Yang, G. Rousse, K. Louise Svane, et al., "Cation Insertion to Break the Activity/Stability Relationship for Highly Active Oxygen Evolution Reaction Catalyst," *Nature Communications* 11 (2020): 1378.

5. S. H. Chang, J. G. Connell, N. Danilovic, et al., "Activity–stability Relationship in the Surface Electrochemistry of the Oxygen Evolution Reaction," *Faraday Discussions* 176 (2014): 125–133.

6. F.-Y. Chen, Z.-Y. Wu, Z. Adler, and H. Wang, "Stability Challenges of Electrocatalytic Oxygen Evolution Reaction: From Mechanistic Understanding to Reactor Design," *Joule* 5 (2021): 1704–1731.

7. A. Mavrič, M. Fanetti, Y. Lin, M. Valant, and C. Cui, "Spectroelectrochemical Tracking of Nickel Hydroxide Reveals Its Irreversible Redox States upon Operation at High Current Density," *ACS Catalysis* 10 (2020): 9451–9457.

8. C. Spöri, J. T. H. Kwan, A. Bonakdarpour, D. P. Wilkinson, and P. Strasser, "The Stability Challenges of Oxygen Evolving Catalysts: Towards a Common Fundamental Understanding and Mitigation of Catalyst Degradation," *Angewandte Chemie International Edition* 56 (2017): 5994–6021.

9. M. Risch, "Upgrading the Detection of Electrocatalyst Degradation during the Oxygen Evolution Reaction," *Current Opinion in Electrochemistry* 38 (2023): 101247.

10. A. Grimaud, K. J. May, C. E. Carlton, et al., "Double Perovskites as a Family of Highly Active Catalysts for Oxygen Evolution in Alkaline Solution," *Nature Communications* 4 (2013): 2439.

11. M. L. Weber, C. Baeumer, D. N. Mueller, et al., "Electrolysis of Water at Atomically Tailored Epitaxial Cobaltite Surfaces," *Chemistry of Materials* 31 (2019): 2337–2346.

12. F. Gunkel, D. V. Christensen, Y. Z. Chen, and N. Pryds, "Oxygen Vacancies: The (in)visible Friend of Oxide Electronics," *Applied Physics Letters* 116 (2020): 120505.

13. A. Wattiaux, J. C. Grenier, M. Pouchard, and P. Hagenmuller, "Electrolytic Oxygen Evolution in Alkaline Medium on La_{1-x} Sr_x FeO_{3-y} Perovskite-Related Ferrites: I . Electrochemical Study," *Journal of the Electrochemical Society* 134 (1987): 1714–1718.

14. S. She, J. Yu, W. Tang, et al., "Systematic Study of Oxygen Evolution Activity and Stability on La_{1-x} Sr_x $FeO_{3-\delta}$ Perovskite Electrocatalysts in Alkaline Media," *ACS Applied Materials & Interfaces* 10 (2018): 11715–11721.

15. V. Celorrio, L. Calvillo, G. Granozzi, A. E. Russell, and D. J. Fermin, "A MnO_3 (A = Sr, La, Ca, Y) Perovskite Oxides as Oxygen Reduction Electrocatalysts," *Topics in Catalysis* 61 (2018): 154–161.

16. Y. Dessie, S. Tadesse, R. Eswaramoorthy, and B. Abebe, "Recent Developments in Manganese Oxide Based Nanomaterials with Oxygen Reduction Reaction Functionalities for Energy Conversion and Storage Applications: A Review," *Journal of Science: Advanced Materials and Devices* 4 (2019): 353–369.

17. H. Kozuka, K. Ohbayashi, and K. Koumoto, "Electronic Conduction in La-Based Perovskite-Type Oxides," *Science and Technology of Advanced Materials* 16 (2015): 026001.

18. J. Suntivich, K. J. May, H. A. Gasteiger, J. B. Goodenough, and Y. Shao-Horn, "A Perovskite Oxide Optimized for Oxygen Evolution Catalysis from Molecular Orbital Principles," *Science* 334 (2011): 1383–1385.

19. L.-B. Liu, C. Yi, H.-C. Mi, et al., "Perovskite Oxides Toward Oxygen Evolution Reaction: Intellectual Design Strategies, Properties and Perspectives," *Electrochemical Energy Reviews* 7 (2024): 14.

20. Lakhanlal and M. Caspary Toroker, "Filling the Gaps on the Relation Between Electronic Conductivity and Catalysis of Electrocatalysts for Water Splitting Using Computational Modelling," *Current Opinion in Electrochemistry* 40 (2023): 101342.

21. Y. Cheng, A. S. Raman, J. Paige, et al., "Enhancing Oxygen Exchange Activity by Tailoring Perovskite Surfaces," *The Journal of Physical Chemistry Letters* 10 (2019): 4082–4088.

22. M. L. Weber, G. Lole, A. Kormanyos, et al., "Atomistic Insights into Activation and Degradation of $La_{0.6}Sr_{0.4}CoO_{3-\delta}$ Electrocatalysts under Oxygen Evolution Conditions," *Journal of the American Chemical Society* 144 (2022): 17966–17979.

23. J. Li and J. Gong, "*Operando* Characterization Techniques for Electrocatalysis," *Energy & Environmental Science* 13 (2020): 3748–3779.

24. Y. Yang, J. Feijóo, V. Briega-Martos, et al., "Operando Methods: A New Era of Electrochemistry," *Current Opinion in Electrochemistry* 42 (2023): 101403.

25. A. R. Akbashev, V. Roddatis, C. Baeumer, T. Liu, J. T. Mefford, and W. C. Chueh, "Probing the Stability of $SrIrO_3$ during Active Water Electrolysis *via Operando* Atomic Force Microscopy," *Energy & Environmental Science* 16 (2023): 513–522.

26. J. T. Mefford, A. R. Akbashev, M. Kang, et al., "Correlative Operando Microscopy of Oxygen Evolution Electrocatalysts," *Nature* 593 (2021): 67–73.

27. F. Hausen, *Advanced Analytical Methods in Tribology*, ed. M. Dienwiebel and M.-I. De Barros Bouchet (Springer International Publishing, 2018), 247–271.

28. A. Kaus, B. Ying, Z. Teng, et al., "Transient Surface Degradation of LSCO and LSFO during OER in Alkaline Electrolyte under Dynamic Cycling Conditions," *ACS Catalysis* 15 (2025): 13768–13777.

29. J. E. Sader, J. W. M. Chon, and P. Mulvaney, "Calibration of Rectangular Atomic Force Microscope Cantilevers," *Review of Scientific Instruments* 70 (1999): 3967–3969.

30. E. Meyer, H. J. Hug, and R. Bennewitz, *Scanning Probe Microscopy* (Springer Berlin Heidelberg, 2004).

31. O. Scholder, pySPM, version 0.6.2, *Zenodo*, 2019, https://doi.org/10.5281/ZENODO.998575, see https://github.com/scholi/pySPM for information on Python library and its installation .

32. D. Nečas and P. Klapetek, "Gwyddion: An Open-Source Software for SPM Data Analysis," *Open Physics* 10 (2012): 181–188.

33. M. Rabe, C. Toparli, Y.-H. Chen, O. Kasian, K. J. J. Mayrhofer, and A. Erbe, "Alkaline Manganese Electrochemistry Studied by In Situ and *Operando* Spectroscopic Methods – Metal Dissolution, Oxide Formation and Oxygen Evolution," *Physical Chemistry Chemical Physics* 21 (2019): 10457–10469.

34. K. J. May, C. E. Carlton, K. A. Stoerzinger, et al., "Influence of Oxygen Evolution during Water Oxidation on the Surface of Perovskite Oxide Catalysts," *The Journal of Physical Chemistry Letters* 3 (2012): 3264–3270.

35. L. Heymann, I. C. G. Van Den Bosch, D. H. Wielens, et al., "Revealing the Intrinsic Oxygen Evolution Reaction Activity of Perovskite Oxides across Conductivity Ranges Using Thin Film Model Systems," *ACS Applied Materials & Interfaces* 17 (2025): 21110–21121.

36. J.-W. Zhao, Y. Li, D. Luan, and X. W. Lou, "Structural Evolution and Catalytic Mechanisms of Perovskite Oxides in Electrocatalysis," *Science Advances* 10 (2024): eadq4696.

37. J. T. Mefford, X. Rong, A. M. Abakumov, et al., "Water Electrolysis on $La_{1-x}Sr_xCoO_{3-\delta}$ Perovskite Electrocatalysts," *Nature Communications* 7 (2016): 11053.

38. N.-S. Park, M.-W. Kim, S. C. Langford, and J. T. Dickinson, "Atomic Layer Wear of Single-Crystal Calcite in Aqueous Solution Using Scanning Force Microscopy," *Journal of Applied Physics* 80 (1996): 2680–2686.

39. E. Gnecco and E. Meyer, *Fundamentals of Friction and Wear* (Springer Berlin Heidelberg, 2007).

40. A. Labuda, F. Hausen, N. N. Gosvami, P. H. Grütter, R. B. Lennox, and R. Bennewitz, "Switching Atomic Friction by Electrochemical Oxidation," *Langmuir* 27 (2011): 2561–2566.

41. C. Tian, C. Maheu, X. Huang, et al., "Evaluating the Electronic Structure and Stability of Epitaxially Grown Sr-Doped $LaFeO_3$ Perovskite Alkaline O_2 Evolution Model Electrocatalysts," *RSC Applied Interfaces* 2 (2025): 122–129.

42. B. Han, A. Grimaud, L. Giordano, et al., "Iron-Based Perovskites for Catalyzing Oxygen Evolution Reaction," *Journal of Physical Chemistry C* 122 (2018): 8445–8454.

43. J. Scholz, M. Risch, G. Wartner, C. Luderer, V. Roddatis, and C. Jooss, "Tailoring the Oxygen Evolution Activity and Stability Using Defect Chemistry," *Catalysts* 7 (2017): 139.

44. B. Messaoudi, S. Joiret, M. Keddam, and H. Takenouti, "Anodic Behaviour of Manganese in Alkaline Medium," *Electrochimica Acta* 46 (2001): 2487–2498.

45. L. Köhler, L. Szabadics, C. Jooss, and M. Risch, "Peroxide Yield of the (001) $La_{0.6}Sr_{0.4}MnO_3$ Surface as a Bifunctional Electrocatalyst for the Oxygen Reduction Reaction and Oxygen Evolution Reaction in Alkaline Media," *Batteries & Supercaps* 2 (2019): 364–372.

Supporting Information

Additional supporting information can be found online in the Supporting Information section. **Supporting Fig. S1:** X-ray diffractograms of LSCO (blue), LSFO (green), and LSMO (red) in (001) orientation grown on Nb:STO (001). Please consider that due to the highest intensity of (002) in comparison to (001), the (002) reflections are provided. For the full span of XRD, please refer to Ref. 1. **Supporting Fig. S2:** (a,b) topography of LSCO in air and at OCV, respectively; (c,d) height cross-section of LSCO in air and at OCV, respectively. **Supporting Fig. S3:** (a–c) Topography at OCV after 30 CVs of LSCO, LSFO, and LSMO, respectively. with numbers 1 and 2 indicated cross-sections taken on ACR; (d–f) respective cross-sections over time of 30 CV scans. **Supporting Fig. S4:** (a–c) Schematic of drift direction to compare drift direction between the first cycle and last cycle frame for LSCO, LSFO, and LSMO, respectively.